



# Broadband terahertz radiation from two-color mid- and far-infrared laser filaments in air

Alisée Nguyen, Pedro González de Alaiza Martínez, Illia Thiele, Stefan Skupin, Luc Bergé

## ► To cite this version:

Alisée Nguyen, Pedro González de Alaiza Martínez, Illia Thiele, Stefan Skupin, Luc Bergé. Broadband terahertz radiation from two-color mid- and far-infrared laser filaments in air. *Physical Review A : Atomic, molecular, and optical physics* [1990-2015], 2018, 97 (6), 10.1103/PhysRevA.97.063839 . hal-01818373

**HAL Id: hal-01818373**

**<https://hal.science/hal-01818373>**

Submitted on 19 Jun 2018

**HAL** is a multi-disciplinary open access archive for the deposit and dissemination of scientific research documents, whether they are published or not. The documents may come from teaching and research institutions in France or abroad, or from public or private research centers.

L'archive ouverte pluridisciplinaire **HAL**, est destinée au dépôt et à la diffusion de documents scientifiques de niveau recherche, publiés ou non, émanant des établissements d'enseignement et de recherche français ou étrangers, des laboratoires publics ou privés.

# Broadband THz radiation from two-color mid- and far-infrared laser filaments in air

Alisée Nguyen,<sup>1,\*</sup> Pedro González de Alaiza Martínez,<sup>2</sup> Illia Thiele,<sup>3</sup> Stefan Skupin,<sup>4</sup> and Luc Bergé<sup>1</sup>

<sup>1</sup>CEA, DAM, DIF, 91297 Arpaçon, France

<sup>2</sup>Univ. Bordeaux - CNRS - CEA, Centre Lasers Intenses et Applications, UMR 5107, 33405 Talence, France

<sup>3</sup>Department of Physics, Chalmers University of Technology, SE-412 96 Göteborg, Sweden

<sup>4</sup>Institut Lumière Matière, UMR 5306 Université Lyon 1 - CNRS, Université de Lyon, 69622 Villeurbanne, France

(Dated: May 4, 2018)

We study THz emission by two-color femtosecond filaments in air using pump wavelengths  $\lambda_0$  from 0.8 to 10.6  $\mu\text{m}$ . Comprehensive three-dimensional numerical simulations show that tens-of-centimeter long filaments created by a 10.6- $\mu\text{m}$  pump pulse can produce mJ energy yields and GV/m field strengths, while the laser-to-THz conversion efficiency exceeds the percent level. Changing temperature and humidity conditions reveals a surprisingly high stability of the THz spectra against different weather conditions. We also examine the role of many-body Coulomb effects on ionization. This additional plasma source promotes longer filaments that act as efficient THz emitters.

Terahertz (THz) science is attracting a broad interest because of its ability to detect many molecular fingerprints through non-invasive spectroscopy methods [1]. Efficient laser-based THz sources rely on the nonlinear polarization in  $\chi^{(2)}$  crystals [2] or photocurrents in gas-plasma [3]. A well-known technique is to focus a two-color (2C) femtosecond light pulse, composed of a fundamental pulse (FH) and its second harmonic (SH), into air. From the resulting plasma, THz radiation develops high field strengths and broad spectra, even remotely [4] with no limitation due to laser damage. Recent studies [5, 6] showed that increasing the pump wavelength can enhance the THz conversion efficiency (CE), which is at most limited to  $\sim 10^{-4}$  for a 0.8  $\mu\text{m}$  2C pump pulse. Whereas optical rectification in large-size organic crystals allows to achieve CEs up to the percent level [2], the THz fluence remains below the mJ/cm<sup>2</sup> range. To exceed the mJ limit from small interaction surfaces, increasing the value of the laser wavelength may supply an efficient alternative. Longer laser wavelengths, e.g., 3.9  $\mu\text{m}$  delivered by optical parametric chirped pulse amplification, are nowadays accessible in the femtosecond regime [7]. Ultrafast (100 fs) CO<sub>2</sub> lasers operating at 10.6  $\mu\text{m}$  with energies close to the Joule level are also awaited in the coming years [8, 9]. Therefore, long-range numerical simulations using energetic, sub-ps pulses have been performed in these wavelength domains [10, 11]. [They revealed the possibility to enhance the nonlinear propagation path by copropagating higher harmonics created through carrier wave shock formation \[12\].](#)

In this paper, we focus on intense, broadband THz fields created by long-wavelength pulses. By means of a three-dimensional (3D) unidirectional solver [13], we investigate THz generation in air by 2C femtosecond pulses. The pump wavelength  $\lambda_0$  is varied from 0.8 to 10.6  $\mu\text{m}$ . Our numerical results display evidence of unprecedented THz energy yields and CEs achieved over long distances, in agreement with Local Current (LC) estimations [14]. For CO<sub>2</sub> lasers, we also show that the weather conditions have a surprisingly little im-

pact on the THz spectra. Besides the standard photo-induced field ionization, we finally account for many-body Coulomb ionization in argon, expected to become significant at 10- $\mu\text{m}$  pump wavelength [15, 16]. This additional plasma source efficiently contributes to THz generation earlier in the pulse history.

To start with, we use the LC model [14] to evaluate the performances of long-wavelength optical pulses as potential drivers for THz emission. Here, the THz field  $E_{\text{THz}}$  is extracted from filtering the secondary field  $E_J \propto \partial_t J$  emitted from the free electron current density  $J$  [17]. The filtering frequency is chosen as  $\nu_f = 10$  THz, in order to limit the influence of the pump broadening into the THz spectrum. At moderate laser intensities  $< 10^{15}$  W/cm<sup>2</sup>, the current density is given by a plasma fluid model [3],  $\partial_t J + \nu_c J = e^2 N_e E / m_e$ , where  $e$  and  $m_e$  are the electron charge and mass, respectively;  $\nu_c \approx 2.86 \text{ ps}^{-1}$  is the electron-neutral collision rate [18].  $N_e$  is the density of free electrons governed by

$$\partial_t N_e = \sum_i W_i(E)(N_{a,i} - N_{e,i}), \quad (1)$$

where  $N_{a,i}$  and  $N_{e,i}$  are the initial gas density of species  $i = \text{O}_2, \text{N}_2$ , and their extracted electron density, respectively, so that  $N_e = \sum_i N_{e,i}$ .  $W_i(E)$  is the field-dependent version of the cycle-averaged Perelomov, Popov and Terent'ev (PPT) ionization rate [19] applied for air to 80% of nitrogen and 20% of oxygen with ionization potentials  $U_i(\text{N}_2) = 15.6$  eV and  $U_i(\text{O}_2) = 12.1$  eV. For Ar we will use  $U_i(\text{Ar}) = 15.76$  eV.

We apply the LC model to the local input laser field

$$E(t) = E_0 \sum_{n=1,2} a_n e^{-(2n \ln 2 \frac{t}{\tau})^2} \cos(n\omega_0 t + \phi_n), \quad (2)$$

where the amplitude  $E_0 = \sqrt{2I_0/c\epsilon_0}$  depends on the pump intensity  $I_0$ ,  $\tau = \nu_f^{-1} = 100$  fs is the full-width-at-half-maximum (FWHM) pulse duration,  $\omega_0 = 2\pi c/\lambda_0$  is the FH frequency ( $n = 1$ ),  $a_n$  and  $\phi_n$  are the amplitude

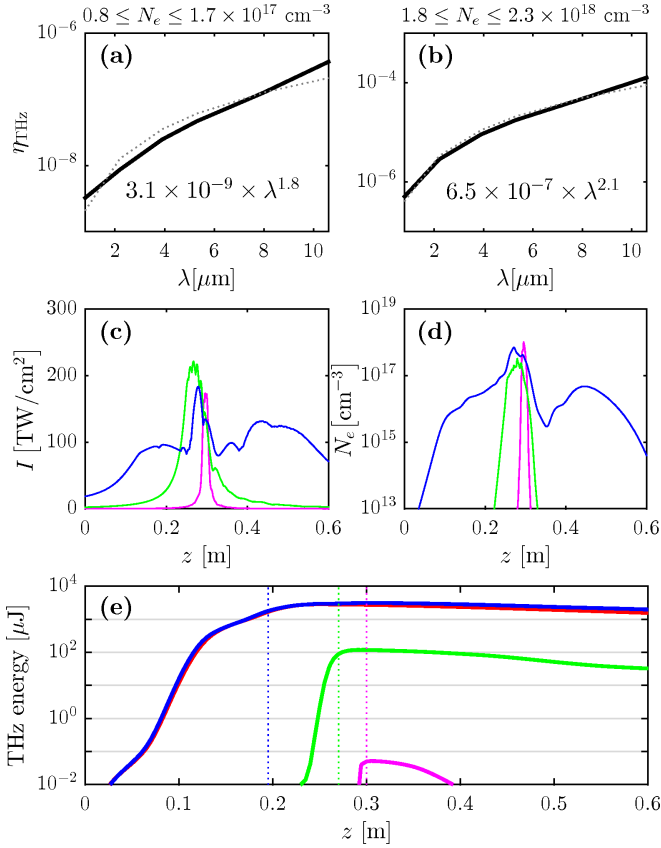


FIG. 1. (a,b) Laser-to-THz CE evaluated in the frequency window  $\nu < 10$  THz from Eq. (1) using the two input fluences (a)  $5 \text{ J}/\text{cm}^2$  and (b)  $10 \text{ J}/\text{cm}^2$  ( $\phi_1 = 0$ ,  $\phi_2 = \pi/2$ ) and producing electron densities that barely vary with the FH wavelength (see top values). Dotted gray curves are fits in  $\lambda^\alpha$ . (c,d,e) Results from 3D UPPE simulations of 2C near- to far-infrared filaments. (c) Maximum intensity along  $z$  using winter HITRAN dispersion for FH pump wavelengths of 0.8 (magenta), 3.9 (green) and 10.6  $\mu\text{m}$  (blue curves). Associated (d) peak electron densities and (e) THz energies [integral over  $(x, y, t)$ ], computed along  $z$  for winter (blue) and summer (red curve) in the case of the 10.6- $\mu\text{m}$  FH. Vertical dotted lines show the distances of maximum THz generation (see text).

coefficient and phase of the  $n$ th harmonic, respectively. We consider 2C pulses with amplitude coefficients  $a_1 = \sqrt{0.9}$ ,  $a_2 = \sqrt{0.1}$  and laser fluences  $U_L = 5 - 10 \text{ J}/\text{cm}^2$ , corresponding to  $I_0 = 100 - 200 \text{ TW}/\text{cm}^2$  mean intensities. The relative phase between the two colors is set to its optimum value of  $\pi/2$  for THz generation by photocurrents [3, 6]. We show in Figs. 1(a,b) the evolution of the THz yield  $\eta_{\text{THz}} = \int_{-\nu_f}^{+\nu_f} |\partial_t \hat{J}|^2 d\nu / [(e^2 N_a / m_e)^2 U_L]$  with the pump wavelength [20], for which we compute the electron density through Eq. (1) for  $\text{O}_2$ . With a 10.6- $\mu\text{m}$  pump wavelength, a gain of about two orders of magnitude can be expected in the THz energy yield compared with a near-IR pump. A tentative scaling in  $\lambda^\alpha$  supports an exponent  $\alpha$  close to 2 [6]. The energy density should thus be readily increased by four orders

$\lambda_0$ [ $\mu\text{m}$ ]/gas	0.8/air	3.9/air	10.6/air	10/argon
$n_2$ [ $10^{-19} \text{ cm}^2/\text{W}$ ]	3.8	3.6	3.3	1.0
$x_K$	0.8	0.8	0.8	0.0
$U_L$ [mJ]	0.494	12.4	100	169.4

TABLE I. Pump wavelengths, Kerr indices, Raman-delayed ratios and input laser energies for air and argon.

of magnitude when multiplying the FH wavelength by a factor 10, first through photocurrents [Fig. 1], second by preserving in the optical beam the same amount of critical powers for self-focusing  $P_{\text{cr}} \propto \lambda_0^2$ . This possibility thus invites us to operate in the filamentation regime [21], for which the larger critical power at long wavelengths renders the self-guiding of high pump energies in a single filament possible, without beam breakup.

To test the previous evaluation, we use the 3D Unidirectional Pulse Propagation Equation (UPPE) [13]:

$$\partial_z \hat{E} = i \sqrt{k^2(\omega) - k_x^2 - k_y^2} \hat{E} + i \frac{\mu_0 \omega^2}{2k(\omega)} \hat{\mathcal{F}}_{\text{NL}}, \quad (3)$$

where  $k(\omega) = n(\omega)\omega/c$  is the wave number with air refraction index  $n(\omega)$ ,  $z$  is the propagation variable and  $\hat{E}(k_x, k_y, z, \omega)$  is the Fourier transform of the electric field. The first term on the right-hand side of Eq. (3) describes linear dispersion and diffraction of the pulse. The second term  $\hat{\mathcal{F}}_{\text{NL}}$  contains the third-order nonlinear polarization  $\hat{P}_{\text{NL}}$ , the electron current  $\hat{J}$  and a loss term due to ionization [21]. Air dispersion is taken from [22], completed with HITRAN data [23, 24] accounting for water vapor and carbon dioxide. The main absorption lines are located at 2.7 and 5.2-7.3  $\mu\text{m}$  for  $\text{H}_2\text{O}$  and 4.2  $\mu\text{m}$  for  $\text{CO}_2$ . Two ground-level weather configurations are examined: either “winter” using a moderate temperature of 15°C and local humidity of 20%, or “summer” with 25°C temperature and 60% humidity. The Kerr index  $n_2$  entering  $P_{\text{NL}}$  is given in Table I with Raman-delayed response ratio  $x_K$  [25, 26]. The number of critical powers,  $P_{\text{cr}} = \lambda_0^2 / 2\pi n_2$ , is kept constant and set to 1.73. Plasma generation proceeds from photoionization initiated by the PPT rate [Eq. (1)], supplemented by the avalanche ionization term  $\mu_0 c e^2 \nu_c I N_e / [U_i m_e (\nu_c^2 + \omega^2)]$ , which originates from collisions between free electrons and neutrals by inverse Bremsstrahlung.

In our simulations, the input light field ( $z = 0$ ) reads as Eq. (2) multiplied by a transverse Gaussian profile with  $1/e^2$  radius of 2.5 mm that is focused by a converging lens of 30-cm focal length. The initial phases  $\phi_1$  and  $\phi_2$  are set to zero as the phase angle is continuously evolving through Gouy-phase shift and nonlinear propagation effects. Input pulse energies are indicated in Table I. Numerical simulations were performed using a  $15 \times 15 \text{ mm}^2$  transverse box and a  $\sim 4.3 \text{ ps}$  temporal window. As seen from Figs. 1(c,d), peak intensities of  $\sim 200 \text{ TW}/\text{cm}^2$  produce electron densities above  $10^{17} \text{ cm}^{-3}$ . When in-

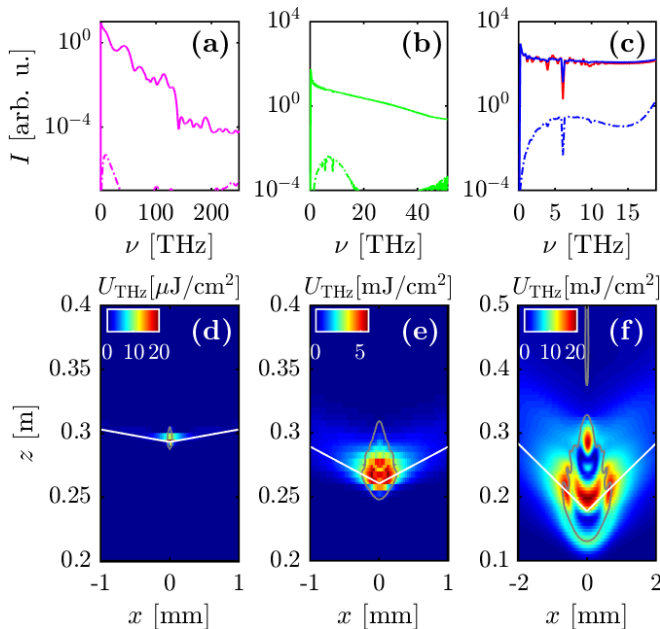


FIG. 2. (a,b,c) Transversally-averaged THz spectra at distances of maximum THz generation (a)  $z = 30$  cm, (b)  $z = 27$  cm and (c)  $z = 19.5$  cm using the same color plot-style as in Figs. 1(c-e). Dash-dotted curves show the same quantities without plasma generation. (d-f) THz pulse fluence in the  $(x, z)$  plane for FH pump wavelengths of (d) 0.8, (e) 3.9 and (f) 10.6  $\mu\text{m}$ . White lines serve as eye guides for the conical emission angles, fitting the curve  $z_{\text{max}}(x)$  such that  $U_{\text{THz}}(x, z_{\text{max}}) = \max_z U_{\text{THz}}(x, z)$ . Plasma transverse isocontours at  $10^{16} \text{ cm}^{-3}$  are indicated by gray lines.

creasing the pump wavelength, longer filaments form (see also [27]). Due to the smaller Rayleigh range, the 10.6- $\mu\text{m}$  pump pulse starts its self-focusing sequence earlier. Figure 1(e) illustrates the THz energy inside part of the numerical box versus the propagation axis. This energy remains below the  $\mu\text{J}$  level for  $\lambda_0 = 0.8 \mu\text{m}$ , but it increases to the 0.1 mJ level for mid-IR pumps and even to 3.1 mJ for far-IR lasers, confirming the 4 orders of magnitude increase expected from the LC model above. The THz CE obtained at 10.6  $\mu\text{m}$  is 3% against 1% at 3.9  $\mu\text{m}$ . Let us notice that the yield curves of Fig. 1(e) decrease instead of saturating to a plateau value, which is mainly due to THz components leaving our finite time window.

To go one step further, Figs. 2(a,b,c) detail the THz spectra computed at the distance of maximum THz production, for which the slope of the THz energy in Fig. 1(e) is the strongest. Because diffraction of THz pulses is very fast, this distance corresponds in most of cases to the location of the maximum on-axis THz intensity. Apart from the impressive increase in the THz spectrum, Fig. 2(c) also evidences for the 10.6  $\mu\text{m}$  pump pulse that augmenting humidity and temperature makes water absorption lines stronger around 3 and 6 THz. However, these absorption zones are spectrally narrow and they do

not visibly reduce the total THz yield, as confirmed by Fig. 1(e). Besides, an important debate has been the role of Kerr-induced four-wave mixing compared to that of photocurrents in laser-driven THz pulse generation [18]. To clear up this point, Figs. 2(a,b,c) compare THz spectra computed until the indicated distances without the plasma terms. The presence of plasma clearly enlarges the spectra by about 3 orders of magnitude and shifts the peak frequencies down to  $\nu_{\text{THz}} < 1$  THz. Hence, plasma generation and related photocurrents — even involving rather low electron densities  $\sim 10^{15-17} \text{ cm}^{-3}$  — remain the key players in THz pulse generation. Figures 2(d,e,h) evidence the broader laser-plasma interaction surfaces engaged at longer FH wavelengths. This is due to the  $\lambda_0$ -dependent increase in the filament waist [27, 28] and so, in the plasma transverse cross-section, which amplifies in turn the THz yield. Also, the conical emission angle of the radiated THz pulses decreases with the FH wavelength: THz waves indeed diffract with angles of 6.2° and 2.3° for  $\lambda_0 = 0.8$  and 3.9  $\mu\text{m}$ , respectively. With a 10.6- $\mu\text{m}$  pump pulse, in contrast, THz waves are emitted nearly on-axis within a 1.2° angle. Hence, they can propagate over a longer distance in the numerical box and offer a better directivity.

Figure 3 displays the entire optical spectrum developed for the three FH wavelengths along the propagation axis, together with optical and THz field patterns at the distance of maximum THz generation. For a near-IR pump, this distance coincides with that of maximum plasma generation, close to focus. When increasing the pump wavelength, high-order harmonics are amplified over a longer coherence length [29] and they form a broader supercontinuum through the plasma nonlinearity, self- and cross-phase modulation [Figs. 3(a,d,g)]. Ionization arises in the rear pulse, but intense pump components remain in the undepleted front pulse [see Figs. 3(b,e,h)]. The THz field is peaked where the pump field is maximum and it increases with  $\lambda_0$  [Figs. 3(c,f,i)].

Another phenomenon appears at 10.6  $\mu\text{m}$ . As shown by Figs. 1(d,e), THz fields are maximum well before maximum plasma generation sets in. At focus, high harmonics mainly go on feeding ionization. However, they do not produce THz waves by photocurrents because their temporal profiles cannot form an efficient, asymmetric field triggering low-frequency radiation. Figure 4 confirms this point: at focus the rear part of the electric field composed of the highest harmonics is intense enough to contribute alone to plasma generation. Ionization steps are created on-axis by high harmonics that can propagate into the plasma, unlike the  $\omega_0$  and  $2\omega_0$  optical components. However, THz generation still proceeds from the residual two colors surviving in the front pulse and forming early density steps. Because the broadest plasma surface extends at  $z = 19.5$  cm [Fig. 2(f)], maximum THz generation takes place at this distance. Much less THz energy is produced at  $z = 30$  cm, as the plasma diameter is de-

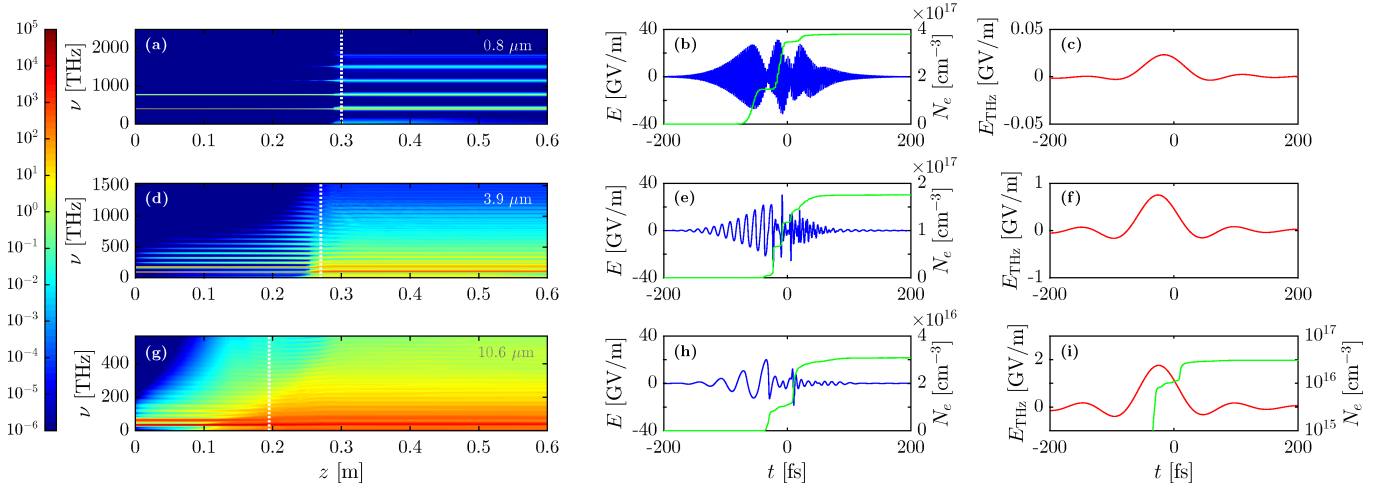


FIG. 3. (a,d,g) Intensity spectra (left colored patterns) along propagation for  $\lambda_0 =$  (a)  $0.8 \mu\text{m}$ , (d)  $3.9 \mu\text{m}$  and (g)  $10.6 \mu\text{m}$ . The vertical dotted lines indicate the distance of maximum THz production. (b,e,h) Corresponding on-axis propagating field (blue curve, left axis) and electron density (green curve, right axis) at maximum THz production. (c,f,i) On-axis THz field obtained by filtering the total electric field  $E$  with a 20th-order Butterworth filter in the frequency window  $\nu < 10 \text{ THz}$ .

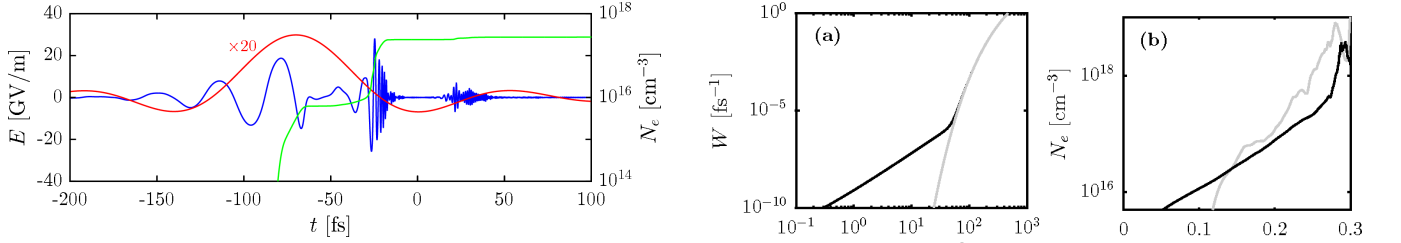


FIG. 4. On-axis electric field for the  $10.6\text{-}\mu\text{m}$  pump pulse at  $z = 30 \text{ cm}$  (blue curve, left axis). The red curve corresponds to the on-axis THz field (strength:  $\times 20$ ). The green curve shows related electron density (right axis).

creased by a factor  $\sim 3.5$ .

Finally, it is compulsory to examine the many-body Coulomb ionization (MBI) effect on THz generation proposed by Schuh *et al.* [15, 16]. Under strong laser field irradiation, excited-state electrons from neighboring atoms are able to collide and thus increase the ionization rate. This effect is all the more relevant as the pump wavelength is large. It manifests at low laser intensities where multi-photon or tunnel ionizations vanish. Therefore, it should be taken into account for far-infrared optical fields. To model it, we use the fit proposed in [16] for a  $10\text{-}\mu\text{m}$  pump wavelength interacting with argon atoms:

$$W_{\text{MBI}}(E) = CE^4 \sqrt{\frac{E^2 + s}{E^2}}, \quad (4)$$

where  $C = 1.1095 \times 10^4 \text{ m}^4/\text{GV}^4$  and  $s = 4.6 \text{ GV}^2/\text{m}^2$ . So, we now turn to an argon gas at ambient pressure and, using Table I's parameters, simulate 100-fs focused pump pulses operating at critical power with a  $1/e^2$  radius of  $3.5 \text{ mm}$ . The MBI rate is added to the PPT rate of Eq. (1), yielding the ionization curve plotted in Fig. 5(a).

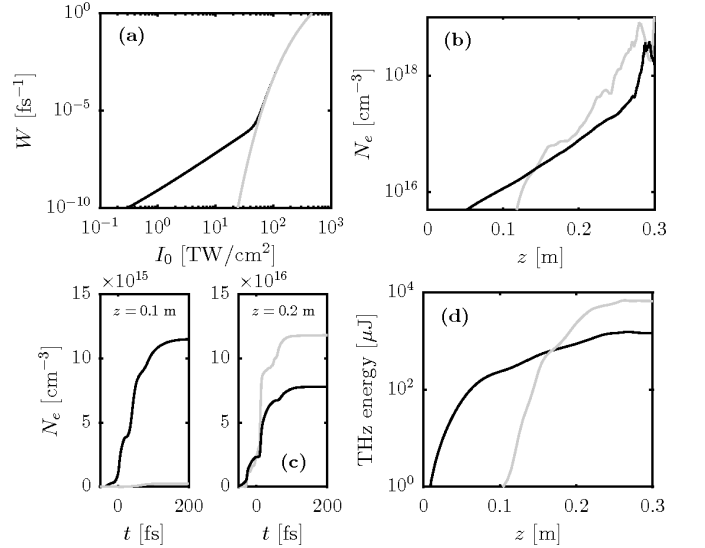


FIG. 5. (a) Ionization rate vs laser intensity with (black lines) or without (gray lines) MBI evaluated from Eq. (2) as input in a 1-bar argon gas. (b) Peak electron density reached along propagation (UPPE simulations with collisional ionization) including (black) or not (gray lines) MBI. (c) Plasma density profiles in time at  $z = 0.1 \text{ m}$  and  $z = 0.2 \text{ m}$ . (d) Associated THz energy yield.

Compared with the PPT rate alone, the MBI rate  $\propto E^4$  is important in the intensity region  $< 20 \text{ TW}/\text{cm}^2$  and allows a more efficient ionization at earlier propagation [see Fig. 5(b)]. Figure 5(c) details the plasma response in time, which is mainly governed by Eq. (4) in the range  $z \leq 10 \text{ cm}$ . This exhibits a steplike increase, which can promote efficient photocurrents although the MBI steps are less sharp than the ones occurring in the tunnel



regime [14] at, e.g.,  $z = 20$  cm. With such plasma contribution, we finally report in Fig. 5(d) that THz emission starts at the very beginning of the propagation range, but it saturates due to accumulated plasma defocusing actions. Without MBI, a THz energy yield of 7-mJ is reached, corresponding to 4% conversion efficiency. With MBI, comparable, although quantitatively smaller values are reached (1.5 mJ THz energy and 0.9% CE).

In summary, we demonstrated by means of numerical simulations that two-color CO<sub>2</sub> laser filaments can provide THz conversion efficiencies above the percent level at moderate laser intensities. Far-infrared filaments are able to self-channel over longer distances and supply energy yields of several mJ. We outlined the effects of weather conditions as well as the influence of many-body ionization. Even if the latter effects may mitigate the conversion efficiency to some extent, they still enable to produce mJ-energetic THz fields over long propagation ranges.

This work was supported by the ANR/ASTRID Project “ALTESSE” # ANR-15-ASTR-0009 and performed using HPC resources from GENCI (Grant # A0020507594). S.S. acknowledges support by the Qatar National Research Fund through the National Priorities Research Program (Grant # NPRP 8-246-1-060).

---

\* alisee.nguyen@cea.fr

- [1] M. Tonouchi, *Nature Photon.* **1**, 97 (2007).
- [2] C. Vicario, B. Monoszlai, and C. P. Hauri, *Phys. Rev. Lett.* **112**, 213901 (2014).
- [3] K. Y. Kim, A. J. Taylor, J. H. Glowina, and G. Rodriguez, *Nature Photon.* **2**, 605 (2008).
- [4] J.-F. Daigle, F. Théberge, M. Henriksson, T.-J. Wang, S. Yuan, M. Châteauneuf, J. Dubois, M. Piché, and S. L. Chin, *Opt. Express* **20**, 6825 (2012).
- [5] M. Clerici, M. Peccianti, B. E. Schmidt, L. Caspani, M. Shalaby, M. Giguère, A. Lotti, A. Couairon, F. Légaré, T. Ozaki, D. Faccio, and R. Morandotti, *Phys. Rev. Lett.* **110**, 253901 (2013).
- [6] A. Nguyen, P. González de Alaiza Martínez, J. Déchard, I. Thiele, I. Babushkin, S. Skupin, and L. Bergé, *Opt. Express* **25**, 4720 (2017).
- [7] D. Kartashov, S. Ališauskas, A. Pugžlys, A. Voronin, A. Zheltikov, M. Petrarca, P. Béjot, J. Kasparian, J.-P. Wolf, and A. Baltuška, *Opt. Lett.* **16**, 3456 (2012).
- [8] I. V. Pogorelsky, M. Babzien, I. Ben-Zvi, J. Skaritka, and M. N. Polyansky, *Nucl. Inst. Meth. Phys. Res. A* **829**, 432 (2016).
- [9] S. Y. Tochitsky, J. J. Pigeon, D. J. Haberberger, C. Gong, and C. Joshi, *Opt. Express* **20**, 13762 (2012).
- [10] N. A. Panov, D. E. Shipilo, V. A. Andreeva, O. G. Kosareva, A. M. Saletsky, H. Xu, and P. Polynkin, *Phys. Rev. A* **94**, 041801 (2016).
- [11] Y. E. Geints and A. A. Zemlyanov, *Appl. Opt.* **53**, 5641 (2014).
- [12] P. Panagiotopoulos, P. Whalen, M. Kolesik, and J. Moloney, *Nature Photon.* **8**, 543 (2015).
- [13] M. Kolesik and J. V. Moloney, *Phys. Rev. E* **70**, 036604 (2004).
- [14] I. Babushkin, W. Kuehn, C. Köhler, S. Skupin, L. Bergé, K. Reimann, M. Woerner, J. Herrmann, and T. Elsaesser, *Phys. Rev. Lett.* **105**, 053903 (2010).
- [15] K. Schuh, J. Hader, J. V. Moloney, and S. W. Koch, *Phys. Rev. E* **89**, 033103 (2014).
- [16] K. Schuh, M. Kolesik, E. M. Wright, J. V. Moloney, and S. W. Koch, *Phys. Rev. Lett.* **118**, 063901 (2017).
- [17] O. D. Jefimenko, *Electricity and Magnetism: An Introduction to the Theory of Electric and Magnetic Fields* (Appleton-Century-Crofts, New York, 1966).
- [18] V. A. Andreeva, O. G. Kosareva, N. A. Panov, D. E. Shipilo, P. M. Solyankin, M. N. Esaulkov, P. González de Alaiza Martínez, A. P. Shkurinov, V. A. Makarov, L. Bergé, and S. L. Chin, *Phys. Rev. Lett.* **116**, 063902 (2016).
- [19] A. M. Perelomov, V. S. Popov, and M. V. Terent'ev, *Sov. Phys. JETP* **23**, 924 (1966).
- [20] A. Nguyen, P. González de Alaiza Martínez, I. Thiele, S. Skupin, and L. Bergé, *New J. Phys.* (2018), in press - DOI: <https://doi.org/10.1088/1367-2630/aaa470>.
- [21] L. Bergé, S. Skupin, R. Nuter, J. Kasparian, and J. P. Wolf, *Rep. Prog. Phys.* **70**, 1633 (2007).
- [22] E. R. Peck and K. Reeder, *J. Opt. Soc. Am. A* **62**, 958 (1972).
- [23] *Hitran on the Web* (2017), <http://hitran.iao.ru/>.
- [24] L. S. Rothman *et al.*, *Journal of Quantitative Spectroscopy and Radiative Transfer* **130**, 4 (2013), HITRAN2012 special issue.
- [25] S. Zahedpour, J. K. Wahlstrand, and H. M. Milchberg, *Opt. Lett.* **40**, 5794 (2015).
- [26] J. J. Pigeon, S. Y. Tochitsky, E. C. Welch, and C. Joshi, *Opt. Lett.* **41**, 3924 (2016).
- [27] Y. E. Geints and A. A. Zemlyanov, *Appl. Opt.*, 1397 (2017).
- [28] L. Bergé, *Opt. Express* **16**, 21529 (2008).
- [29] L. Bergé, J. Rolle, and C. Köhler, *Phys. Rev. A* **88**, 023816 (2013).